Nano Energy 91 (2022) 106654

Contents lists available at ScienceDirect

Nano Energy

journal homepage: www.elsevier.com/locate/nanoen

Ferroelectric P(VDF-TrFE) wrapped InGaAs nanowires for ultralow-power artificial synapses

Pengshan Xie [a], Yulong Huang [b], Wei Wang [a], You Meng [a,c], Zhengxun Lai [a], Fei Wang [a,c], SenPo Yip [d], Xiuming Bu [a], Weijun Wang [a], Dengji Li [a], Jia Sun [b,*], Johnny C. Ho [a,c,d,e,**]

[a] Department of Materials Science and Engineering, City University of Hong Kong, Kowloon 999077, Hong Kong Special Administrative Region
[b] Hunan Key Laboratory for Super-microstructure and Ultrafast Process, School of Physics and Electronics, Central South University, Changsha 410083, Hunan, China
[c] State Key Laboratory of Terahertz and Millimeter Waves, City University of Hong Kong, Kowloon 999077, Hong Kong Special Administrative Region
[d] Institute for Materials Chemistry and Engineering, Kyushu University, Fukuoka 816-8580, Japan
[e] Key Laboratory of Advanced Materials Processing & Mold (Zhengzhou University), Ministry of Education, Zhengzhou 450002, Henan, China

ARTICLE INFO

Keywords:
InGaAs nanowires
Artificial synapse
Ferroelectric polymer
Negative photoconductivity
Associative learning

ABSTRACT

The gallop of artificial intelligence ignites urgent demand on information processing systems with ultralow power consumption, reliable multi-parameter control and high operation efficiency. Here, the poly(vinylidene fluoride-trifluoroethylene) (P(VDF-TrFE)) wrapped InGaAs nanowire (NW) artificial synapses capable to operate with record-low subfemtojoule power consumption are presented. The essential synaptic behaviors are mimicked and modulated effectively by adjusting the thickness of top P(VDF-TrFE) films. Moreover, the long-term depression is realized by applying visible light (450 nm) because of the negative photoconductivity of InGaAs nanowires. Combined with optimal P(VDF-TrFE) films, the synaptic devices have the more linear long-term potentiation/depression characteristics and the faster supervised learning process simulated by hardware neural networks. The Pavlovian conditioning is also performed by combining electrical and infrared stimuli. Evidently, these ultralow-operating-power synapses are demonstrated with the brain-like behaviors, effective function modulation, and more importantly, the synergistic photoelectric modulation, which illustrates the promising potentials for neuromorphic computing systems.

1. Introduction

In the past decade, the rapid development of information and communication technologies have made our human life much more convenient and comfortable [1]. Unsurprisingly, the heavy utilization of artificial intelligence, big data, global network integration and Internet of Things are all constantly challenging the performance limits of von Neumann's classical computer architecture, the mathematics-based system that almost every computer was built on since its first development in 1948 [2–4]. In this way, there is an urgent need to realize a more efficient and low-operating-power processing scheme for large amounts of unstructured data in order to sustain the future technology revolution. Generally, human brains have one of the most sophisticated structures, which can process and store large quantities of data simultaneously with high-speed and ultralow power consumption [5]. Inspired by human brains, the neuromorphic computing technology based on artificial neural network architectures is proposed and rapidly developed [6,7]. Due to the variability of the weight of synaptic connections, the artificial synapses usually have the higher precision and the more robustness in dealing with unstructured data [8,9]. However, these systems will inevitably generate a lot of redundant data during calculation [10], where the associated high-power consumption becomes one of the biggest problems, hindering the further development of the neuromorphic computing technology [11]. It is therefore significant to fabricate the artificial synaptic devices with ultralow power consumption and uncomplicated methods.

Lately, due to the advantages of ferroelectric polymers, including the compatibility with solution processing schemes and flexible substrates, the fatigue-free remnant polarization and controllable polarization intensity, the ferroelectric polymers can control accumulation, depletion

* Corresponding author.
** Corresponding author at: Department of Materials Science and Engineering, City University of Hong Kong, Kowloon 999077, Hong Kong Special Administrative Region.
E-mail addresses: jiasun@csu.edu.cn (J. Sun), johnnyho@cityu.edu.hk (J.C. Ho).

https://doi.org/10.1016/j.nanoen.2021.106654
Received 30 August 2021; Received in revised form 2 October 2021; Accepted 20 October 2021
Available online 26 October 2021

and retention of carriers in the semiconducting channel by polarization switching; hence, great efforts have been made to explore artificial synaptic devices with ferroelectric polymers [12–16]. At the same time, among many candidate device structures and materials, one-dimensional (1D) nanomaterials, such as nanowires (NWs) and nanotubes (NTs), have the analogous topology to tubular axons, which has the great influence on processing data in biological systems [2]. Combined with the characteristics of high surface-to-volume ratio, efficient charge carrier transport and effective light response to specific wavebands, these 1D nanomaterials are widely projected to perform more flexibly to regulate synaptic activities in an ultralow power manner [17–19].

In this work, we propose and demonstrate the artificial synaptic field-effect transistors (FETs) by wrapping InGaAs NWs with P(VDF-TrFE). In specific, two-step chemical vapor deposition (CVD) method was adopted to synthesize highly crystalline InGaAs NWs. The wrap-around ferroelectric P(VDF-TrFE) film was prepared in ambient atmosphere by direct spin-coating. Owing to the high surface-to-volume ratio of InGaAs NWs, the well-defined synaptic functions can be readily achieved through modulating the degree of polarization of the wrap-around ferroelectric P(VDF-TrFE) film according to the electrical stimulus and the different film thickness. Remarkably, subfemtojoule-level energy consumption per synaptic event is realized by these InGaAs NW synaptic devices with wrap-around P(VDF-TrFE) films, which presents the record-low energy consumption among all state-of-the-art artificial synaptic devices. Moreover, because of the negative photoconductivity phenomenon of InGaAs NWs, the fabricated synaptic devices can reliably perform long-term potentiation/depression (LTP/LTD) via both electrical and visible light (450 nm) stimuli, respectively. Notably, the hardware neural network is also simulated for supervised learning, exhibiting the accuracy over 80%. The classical Pavlovian conditioning can as well be achieved by combining the electrical stimulus together with the infrared stimulus (1550 nm). All these results evidently indicate the promising potential of ultralow-power InGaAs NWs artificial synaptic devices for practical utilization in next-generation synaptic electronics.

2. Results and discussion

InGaAs NWs used in this work were synthesized via the two-step catalytic solid-source CVD method reported before [20,21]. Fig. 1a shows the schematic illustration of the CVD step up for the NW synthesis. Once the NW growth finished, scanning electron microscopy (SEM) was first performed on the obtained NWs. It is seen that the NWs are dense, long and thin with smooth surface and uniform diameter along the axial direction (Figs. 1b and S1a). Next, based on the transmission electron microscopy (TEM) findings, the NWs have typical diameters of ~30 nm with spherical catalytic seeds clearly observed at the tips (Fig. 1c), which confirms the vapor-liquid-solid (VLS) growth mechanism of the NWs [22–25]. Energy-dispersive X-ray spectroscopy (EDS) is then used to assess the composition of InGaAs NWs, which determines the composition of $In_xGa_{1-x}As$ with x being about 0.47 (Fig. S1b). The corresponding elemental mappings were also collected on a representative NW, illustrating the homogenous distribution of In, Ga and As along the NW body (Fig. S2). Combined with the obvious lattice fringes with a spacing of 0.34 nm between adjacent lattice planes, corresponding to the <111> dominant direction of the $In_{0.47}Ga_{0.53}As$ NWs (Fig. 1d), high-quality InGaAs are successfully obtained here.

After that, the ferroelectric P(VDF-TrFE) wrapped InGaAs NW artificial synaptic devices were configured in the global back-gate geometry as shown in the device schematic in Fig. 1e. The P(VDF-TrFE) film was fabricated via spin-coating in ambient atmosphere, which wrapped around the InGaAs NW channel and served to modulate the synaptic device behaviors [26]. Fig. S3a and b illustrate the molecular structure of P(VDF-TrFE) and give the SEM image of the device without any P(VDF-TrFE) film, respectively. In fact, it is widely studied that the native oxide on the NW surface would induce charge traps on the channel surface, yielding different hysteresis windows under sweeping with different gate voltage (V_G) [27,28]. Hence, it is essential to investigate this hysteresis effect before depositing the P(VDF-TrFE) film. It is found that our pristine device exhibits the obvious hysteresis window shift under a voltage of pulse of 50 V (Fig. 1f), perfectly consistent with the previous findings in the community. These changes of hysteresis

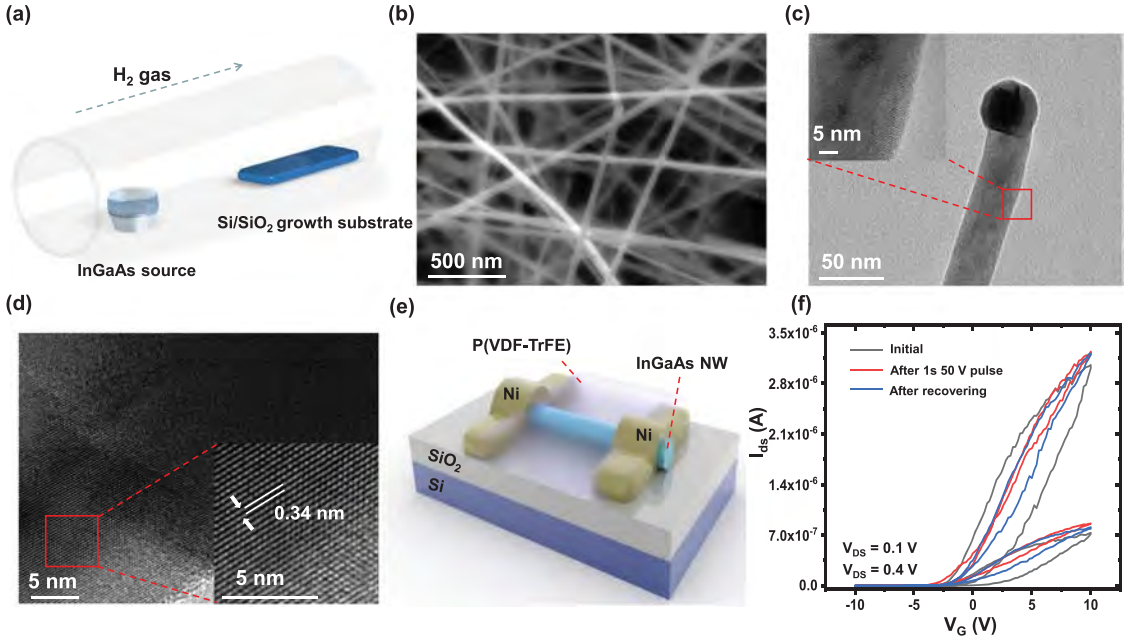

Fig. 1. Growth setup and characterization of obtained NWs and their devices. (a) Schematic illustration of the CVD setup for the NW synthesis. (b) SEM image of the InGaAs NWs grown on Si/SiO_2. (c) TEM image of the InGaAs NW with the inset showing the corresponding high-magnification image of the NW body within the red colored box. (d) HRTEM image of the InGaAs NW. Inset gives the corresponding high-magnification image of the NW region indicated by the red colored box. (e) Schematic illustration of the synaptic device structure. (f) Transfer characteristic curves of the device without any P(VDF-TrFE) film before and after the voltage pulse.

windows are mostly attributed to the charge trapping by native oxides and surface defect states, where the native oxides are clearly observed in the HRTEM images of NWs (Fig. S4) [29,30]. After a large voltage pulse, large amounts of charge carriers would be induced in the channel to fill all the defect states, which causes the narrowing of the hysteresis window. In any case, this charge trapping is temporary and the hysteresis window will recover to its initial condition after a while.

It is as well noted that the thickness of P(VDF-TrFE) film dictates its polarization intensity under the same electrical stimulus [26]. It is therefore critical to evaluate the optimal film thickness of P(VDF-TrFE) for our NW devices. For better characterization and optimization, different thickness of P(VDF-TrFE) films were prepared on Si/SiO_2 in ambient atmosphere and carefully studied. By simply increasing the spin-coating cycles, four different film thickness of 58, 112, 140 and 171 nm were obtained (Fig. S5), while the root-mean-square (RMS) surface roughness of the films was found to increase from 5.45 to 14.5 nm, accordingly (Fig. S6). This slightly increased RMS surface roughness is manageable and anticipated for the thicker films without any noticeable pinholes and cracks. All fabricated films show the intact surface morphology without any noticeable pin holes (Figs. S7 and S8), offering high-quality P(VDF-TrFE) films for subsequent studies.

Technically, when P(VDF-TrFE) films are exploited as gate dielectrics, they often require a relatively large thickness to minimize leakage current, leading to the need of a high gate bias voltage for device operation. Here, by wrapping around the NW with P(VDF-TrFE) as an envelope structure on top of the device, the conflict between leakage current and high operating voltage can be cleverly circumvented [31]. In this case, the electrical performance of InGaAs NW synaptic devices with different P(VDF-TrFE) thickness are cautiously evaluated and depicted in Fig. 2 with the corresponding optical image of the device shown in Fig. S9a. The NW diameters are ensured to be similar across all the devices in order to achieve a fair comparison. It is witnessed that there are obvious changes in the hysteresis window and the transconductance (G_m) of devices with different P(VDF-TrFE) thickness (Figs. 2a–d). The hysteresis window can be simply determined by calculating the voltage difference when the positive and negative sweeping curves are extended down to the x-axis in the transfer characteristic curves of devices. The G_m value of devices is obtained by following the relationship of $G_m = (dI_{DS})/(dV_G)$ at a constant V_{DS}, where I_{DS}, V_G and V_{DS} are the source-drain current, gate voltage and source-drain voltage, respectively. Interestingly, once the 58 nm thick P(VDF-TrFE) film is deposited, the hysteresis window would decrease (Fig. 2a). Simultaneously, X-ray diffraction (XRD) is used to assess the crystallinity of different thickness of P(VDF-TrFE) films. Among all the spectra collected, there are the same obvious peak observed at near $2\theta = 20^\circ$, corresponding to the β-phase domain of P(VDF-TrFE) (Fig. S9b) [15]. In contrast to the α and γ phase, the molecular dipoles of the β-phase are all well aligned in the same direction, thereby demonstrating a large spontaneous polarization [32]. Also, as the film thickness increases, the peak intensity is found to increase correspondingly, indicating the better film crystallinity and hence the stronger polarization under the same stimulation of V_G bias. When the P(VDF-TrFE) film is very thin, the strength of ferroelectric polarization is inconspicuous, mainly playing a role in passivating the surface defect states of NW channels such that the hysteresis window and G_m value would decrease and increase, respectively, as compared with the devices without any P(VDF-TrFE) films (Fig. 2a) [27,33]. As the film goes thicker, the polarization effect becomes more dominant, which induces the widening of the hysteresis window. Fig. S10 shows the transfer characteristic curves of devices with thick P(VDF-TrFE) films in the semi-logarithmic scale, clearly demonstrating the increase of hysteresis window and the same on/off current ratio of $\sim 10^5$.

As compared with the previous works of using P(VDF-TrFE) films as gate dielectrics, the P(VDF-TrFE) wrapped NW devices are found to have the clockwise hysteresis windows, instead of the counter-clockwise ones [34,35]. As depicted in the schematic diagrams in Fig. S11, for $V_G = 0$, there is no electric field externally applied from the gate such that the molecular dipoles would disorderly distribute in the P(VDF-TrFE) film (Fig. S11a). When $V_G = -10$ V, the positively charged ends of the dipoles would get attracted and arranged downwards (Fig. S11b). This is a kind of effective V_G enhancement for n-type semiconductors with additional carriers induced in the NW channel; therefore, the threshold voltage (V_{th}) shifts to the negative voltage direction and the G_m values increase correspondingly (Figs. 2b–d). On the contrary, at $V_G = 10$ V, the arrangement of molecular dipoles is reversed, swapping up and down and contributing to the effective V_G reduction for n-type devices (Fig. S11c). The electrons are then quickly depleted in the NW channel, resulting in the larger clockwise hysteresis window [26,36]. The transfer characteristic curves of the devices with different P(VDF-TrFE) thickness and V_G measurement ranges are also shown in Figs. 2e and f as well as

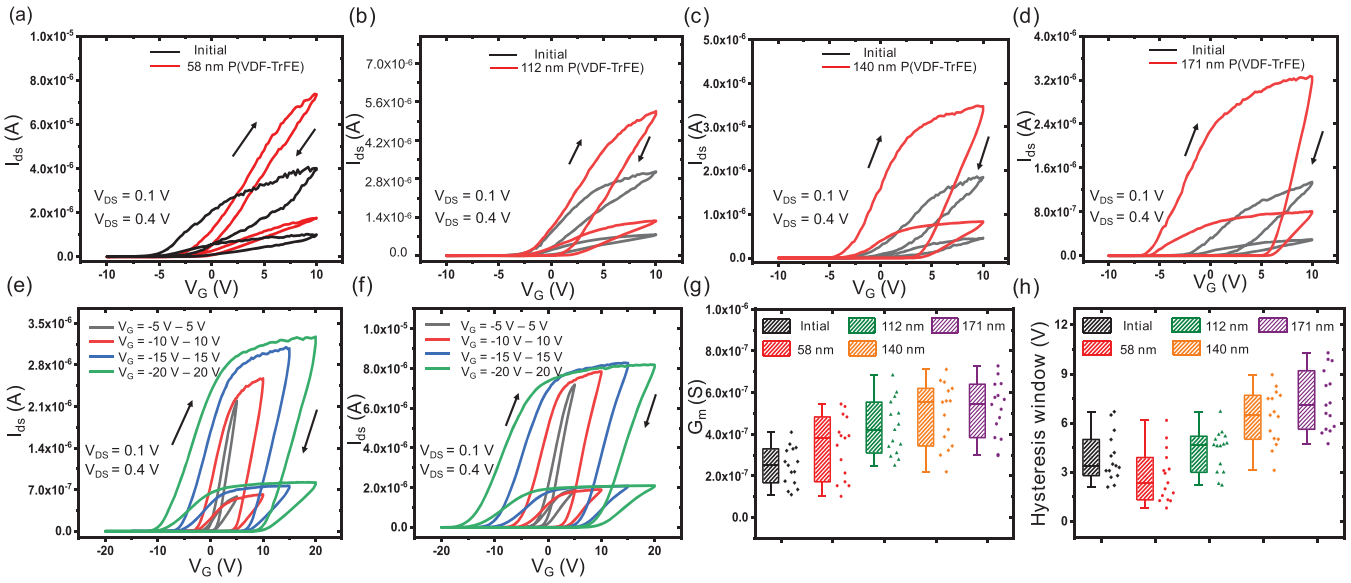

Fig. 2. Electrical studies of P(VDF-TrFE) wrapped InGaAs NW synaptic devices. (a)-(d) Transfer characteristic curves of synaptic devices with different P(VDF-TrFE) thickness. Transfer characteristic curves with different V_G measurement ranges with (e) 140 nm and (f) 171 nm thick P(VDF-TrFE) films. Statistical data of (g) G_m and (h) hysteresis window of the synaptic devices with different P(VDF-TrFE) thickness.

Fig. S12a. Moreover, Fig. S12b depicts the transfer characteristic curves of the device with a 140 nm thick P(VDF-TrFE) film when the larger V_G biases are applied. It is explicit that the larger V_G measurement range causes a stronger polarization electric field in P(VDF-TrFE), which yield the more obvious V_G enhancement in the negative gate bias and V_G reduction in the positive gate bias [37]. In virtue of the advantages of 1D NW and top envelope structures, a relatively thin P(VDF-TrFE) film can be employed to effectively modulate the synaptic device in a low-operating-voltage manner without concerning about the leakage current. The statistical results of G_m and hysteresis widow as a function of different P(VDF-TrFE) thickness are as well shown in Figs. 2g and h. The corresponding hysteresis window decreases first and then increases with the average value changing from 3.8 V (initial) to 7.4 V (171 nm thick film). It is perfectly consistent with the previous conclusion that the thinnest P(VDF-TrFE) film is mainly for the surface passivation of NW channels while the polarization modulation effect would enhance with the increasing film thickness. The statistical data of G_m and hysteresis widow with different P(VDF-TrFE) thickness are also presented in Fig. S13.

In biological synapses, the presynaptic terminal typically receives signals with different strengths and induce the changes of potential in the postsynaptic terminal through a neurotransmitter [38]. Owing to the features of remanent polarization and coercive field in ferroelectric materials, the P(VDF-TrFE) wrapped InGaAs NW artificial synaptic FETs are demonstrated to successfully mimic the behaviors of a biological synapse. The presynaptic spikes are applied through the V_G pulse while the postsynaptic output current (PSC) will be triggered by the polarized P(VDF-TrFE) film. As shown in Fig. S11b, when a negative V_G pulse is applied, the P(VDF-TrFE) film will be polarized accordingly. The rise of the PSC with different V_G is then corresponded to the excitatory postsynaptic current (EPSC) behavior [13]. To be specific, Fig. 3a illustrates the schematic of a biological synapse, whereas Fig. 3b shows the EPSC responses of the NW synaptic devices with a 112 nm thick P(VDF-TrFE) film. The duration of pulse (t_d) and the V_{DS} bias are fixed at 1 ms and 0.4 V, respectively. It is obvious that the increasing amplitude of V_G yields the rapid increase in EPSC, which is consistent with the synaptic behavior. With regard to the retention capability of the devices, two essential synaptic functions can be categorized into short-term plasticity (STP) and long-term plasticity (LTP) by a temporal or persistent change in the synaptic weight [39]. When a pulse of −5 V for 1 ms is applied to the gate, EPSC rises followed by a quick decay to its initial state in a few seconds, indicating the STP characteristics. Further increasing the amplitude of the gate pulse would make the higher EPSC together with the increase of the relaxation time to tens of seconds, designating the transition from STP to LTP [40]. In order to emulate the continuous change of weight in the successive neural activity, paired-pulse facilitation (PPF) is introduced [41]. PPF demonstrates that synapses can inherit and adjust the weight based on the time between paired spikes. In this case, two consecutive presynaptic V_G spikes (1 ms, −10 V) with the interspike interval (ΔTime) changing from 100 ms to 800 ms are applied to mimic the PPF behavior in the NW synaptic device with a 112 nm thick P(VDF-TrFE) film (Fig. S14). As depicted in Fig. 3c, EPSC triggered by the second V_G spike (ΔTime = 100 ms) is obvious larger than that induced by first spike, which is a characteristic indication of the PPF behavior. This PPF phenomenon observed in the ferroelectric P(VDF-TrFE) wrapped InGaAs NW FET is attributed to the polarization accumulation of ferroelectric materials. The ratio of the two different EPSC peaks (A2/A1) can then be used to define the PPF index for the device integrated with a 112 nm thick P(VDF-TrFE) film. This PPF index is plotted as a function of ΔTime and shown in Fig. 3d. It is revealed that the PPF index would decrease with the longer ΔTime of paired spikes and the maximum PPF index value is found to be 117%. In the nervous system, the pulse interval dependent decay of the PPF index can be expressed utilizing a double exponential decay function as presented in the inset of Fig. 3d [42]. The y_0 is the PPF index when the pulse interval approaches to infinity. C_1 and C_2 are the initial facilitation magnitudes of the respective phases. The τ_1 and τ_2 are the decay constant of the rapid phase and the slow phase, respectively. The equation is used to fit the measured pulse-interval dependence of the PPF, where τ_1 and τ_2 are determined to be 92 ms and 113 ms, accordingly. All these indicate that the PPF effect can be successfully mimicked by the ferroelectric P(VDF-TrFE) wrapped InGaAs NW FET.

As discussed above, the thicker P(VDF-TrFE) film would bring the stronger ferroelectric electric field under the same electrical stimulation. The EPSC measurement of the device with a 140 nm P(VDF-TrFE) film are then shown in Fig. 3e and f. It is clear that the more effective modulation of the NW synaptic FET is realized here. In explicit, when $V_G > -14$ V, the relaxation time of EPSC is about hundreds of seconds,

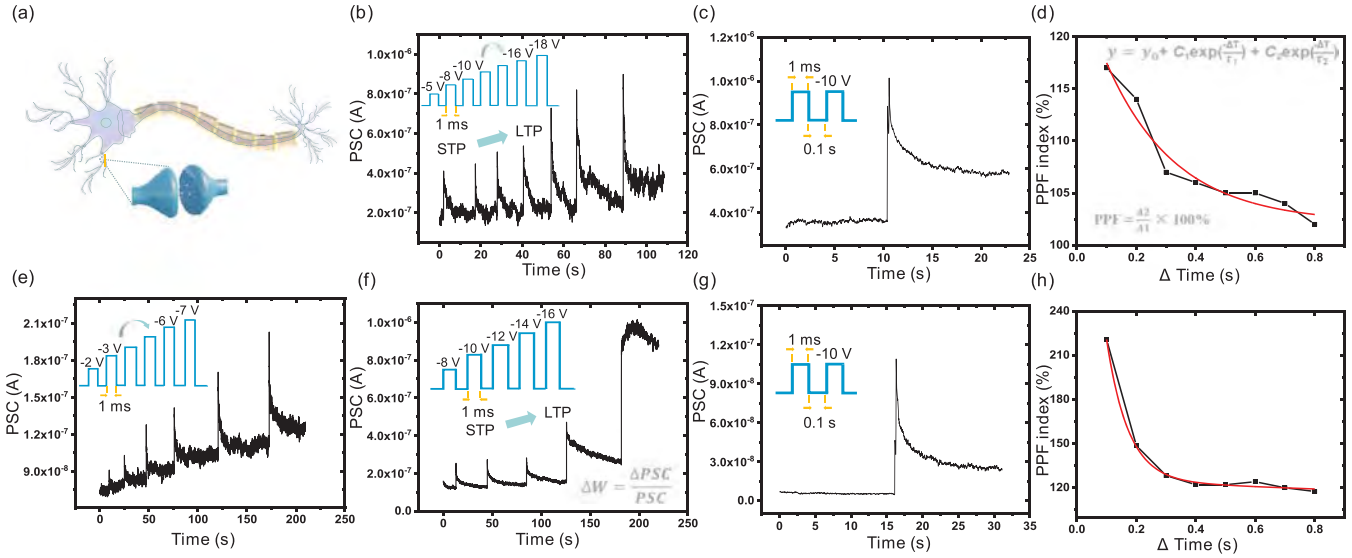

Fig. 3. Synaptic behaviors mimicked in the P(VDF-TrFE wrapped InGaAs NW artificial synapses. (a) Schematic illustration of the biological synapse. (b) EPSC of the synaptic device with the 112 nm thick P(VDF-TrFE) film, demonstrating the typical transformation from STP to LTP. (c) PPF behaviors of the typical InGaAs NW synaptic device with the 112 nm thick P(VDF-TrFE) film. (d) Corresponding PPF index as a function of different pulse intervals. (e) and (f) EPSC of the synaptic device with the 140 nm thick P(VDF-TrFE) film with different V_G pulses. (g) PPF of the synaptic device with the 140 nm thick P(VDF-TrFE) film. (h) Corresponding PPF index as a function of different pulse intervals.

which demonstrates the strong transformation from STP to LTP. The synaptic weight change (ΔW) can be defined as ΔW = ΔPSC/PSC, where ΔPSC is the difference of the current before and after applying the pulses [40]. The ΔW parameter of the devices with two different thickness of P(VDF-TrFE) films is illustrated in Fig. S15. In particular, the ΔPSC value is determined by the difference between the current obtained one second before and five seconds after the pulse. Evidently, the synaptic device with the thicker ferroelectric film has the larger weight change because of the stronger polarization. In addition, the PPF behavior of the device with a 140 nm thick P(VDF-TrFE) film is given in Fig. 3g. When ΔTime = 100 ms, the maximum PPF index value reaches 221%, which is much higher than the device with the thinner ferroelectric film, showing the stronger modulation effect. Besides, the details of two consecutive presynaptic V_G spikes (1 ms, −10 V) with ΔTime changing from 100 ms to 800 ms are also depicted in Fig. S16. The τ_1 and τ_2 parameters are extracted with the same equation in Fig. 3d with the value determined as 100 ms and 160 ms, respectively. By mimicking the biological nervous system, the artificial synapses can modulate the synaptic weight to realize the spike-driven brain-inspired computing systems [43]. However, at present, a relatively large power consumption requirement impedes the development of brain-like computing with artificial synapses. The energy consumption for a single spike event can be estimated as $E = I_{peak} \times t \times V$, where I_{peak} is the peak current flowing across the device, t is the time width of the synaptic event and V is the drain voltage [44]. In a particular case as shown in Fig. S17, the energy consumption of a PPF event is estimated to be ~ 1.78 fJ with V_{DS} = 0.1 mV and fixed V_G spikes (1 ms, −5 V). Remarkably, subfemtojoule power consumption of ~ 0.84 fj per synaptic event is also realized, which is the record-low energy consumption among all state-of-the-art artificial synaptic devices with ferroelectric functional materials. This ultralow energy dissipation of ferroelectric P(VDF-TrFE) wrapped InGaAs NW devices is far below than that of human brain synapses (10 fJ per synaptic event) and other hardware-based artificial synapses especially using P(VDF-TrFE) as a functional layer (Table S1) [3,11,12,15,16,45–51]. The such low energy consumption realized by this ferroelectric functional layer wrapped NW device is possibly due to the ultrahigh surface-to-volume ratio of the NW as mentioned before. Combining with the advantages of wrapped P(VDF-TrFE) film, the modulation effect of ferroelectric film is more sensitive and efficient than the conventional layer-by-layer structure. The high carrier mobility of InGaAs NWs and high on/off current ratio of devices are also the critical factors for devices capable to operate at this ultralow power consumption. In future, the device channel length can be further shrunk below the current design of 2 μm in order to reduce the energy dissipation [52].

Interestingly, when the thickness of P(VDF-TrFE) film reaches 171 nm, the increasing polarization brings the synaptic devices the stronger memory effect. As demonstrated in Fig. 4a, when the consecutive V_G spikes (100 ms, −10 V) with ΔTime = 5 s are applied, EPSC increases in a step-like manner, which means the synaptic weight rises linearly. Besides, different amplitudes of V_G spike are applied to evaluate the EPSC behavior of the device (Fig. 4b). Once V_G spikes change from −5 to −20 V with a fixed t_d = 100 ms, EPSC decays slowly and has the longer relaxation time than the devices with thinner P(VDF-TrFE) films. After 20 s relaxation, EPSC decays for 14%, 19%, 41% and 57% with the V_G spikes changing from −20 to −5 V, respectively. Furthermore, the human memory model is also mimicked by the device with the 171 nm thick P(VDF-TrFE) film. Fig. 4c demonstrates the EPSC behavior triggered by a V_G spike (1 s, −10 V). After the stronger stimulation is applied, the relaxation time of wrapped P(VDF-TrFE) film NW synaptic FET becomes longer, which has many similarities to the memory loss in biological systems. Importantly, the curve fitting result indicates the current decay process being consistent well with the Kohlrausch stretched exponential function (Fig. S18) [41,53,54]. However, the

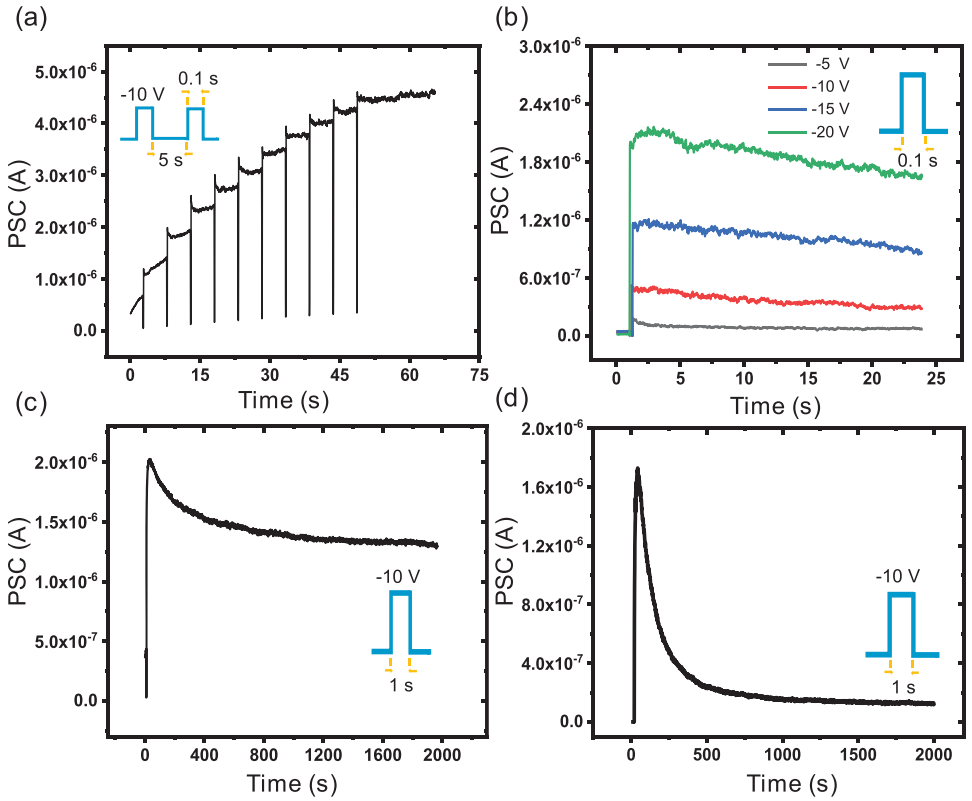

Fig. 4. Mimicking memory behaviors of the thicker P(VDF-TrFE) wrapped InGaAs NW artificial synapses. (a) EPSC of the device (171 nm thick P(VDF-TrFE)) with successive V_G spikes (−10 V, 0.1 s and 5 s interval). (b) EPSC of the device (171 nm thick P(VDF-TrFE)) with a single V_G spike with different amplitudes from − 5 V to − 20 V. EPSC of the devices with (c) 171 and (d) 140 nm thick P(VDF-TrFE) films after a single V_G spike (−10 V, 1 s).

synaptic device with the 140 nm thick P(VDF-TrFE) film exhibits a completely different charge storage capacity under the same V_G spike (1 s, −10 V). As illustrated in Fig. 4d, EPSC has an obvious decay after applying the presynaptic spike and the current is dropped by 72% after 200 s. These results demonstrate that the thickness of wrapped P(VDF-TrFE) film is crucial to achieve the brain-like function. The synaptic device with the 140 nm thick P(VDF-TrFE) film is more sensitive and has the better modulation capacity because of the appropriate polarization intensity. Once the thickness of the ferroelectric film increases to 171 nm, the NW synaptic device yields the stronger memory functions. It is attainable to mimic different brain-like functions through adjusting the thickness of wrapped P(VDF-TrFE) films without concerning about the leakage current.

It is intriguing that 1D NWs have many unusual photoelectric properties, where negative photoconductivity (NPC) is one of the most widely investigated phenomena [55,56]. The underlying mechanisms of NPC are mainly attributed to light-assisted hot electron trapping in the surface oxide, which severe as carrier scattering centers [57,58]. In contrast to many artificial photoelectronic synapses where light stimulation is always used as presynaptic stimulation to trigger the positive EPSC, the LTD can be simply realized through successive light spikes with the NPC phenomenon in our InGaAs NW synaptic devices here. In order to investigate the LTP/LTD characteristics of the P(VDF-TrFE) wrapped InGaAs NW artificial synapses, 100 excitatory and 100 inhibitory spikes are applied to the devices. Fig. 5a demonstrates the EPSC of synaptic device with a 140 nm thick P(VDF-TrFE) film triggered and depressed by successive 100 electrical spikes. Among them, the potentiation of synaptic weight is realized by negative V_G spikes (−10 V, t_d = 1 ms, ΔTime = 1 s) while positive V_G spikes (10 V, t_d = 1 ms, ΔTime = 1 s) can achieve the depression of weight. The insets give the two detailed images of weight enhancement and suppression. Owing to the NPC phenomenon of InGaAs NWs, the P(VDF-TrFE) wrapped InGaAs NW artificial synapses can realize the LTD through visible-range light pulses. As depicted in Fig. 5b, 100 continuous 450 nm visible light pulses are adopted (8 mW, t_d = 0.5 s, ΔTime = 0.5 s) to achieve the LTD. The photoresponse of the synaptic devices with a 140 nm thick P(VDF-TrFE) film is also investigated in Fig. S19**.** It is believed that the wavelength of the light source plays an important role in NPC phenomenon. Therefore, light with a shorter wavelength is easier to induce the NPC behavior.

In general, hardware neural networks (HNNs) are systems designed to carry out neural architectures and to implement leaning algorithms. In this case, it is important to explore the LTP/LTD characteristics of our devices under different P(VDF-TrFE) film thickness as well as varied electrical/optical stimulations. As shown in Fig. 5c, the synaptic devices with different P(VDF-TrFE) thickness and various depression stimuli are modulated by 100 continuous potentiation/depression pulses. Besides, the synaptic device with the 140 nm thick P(VDF-TrFE) film is also

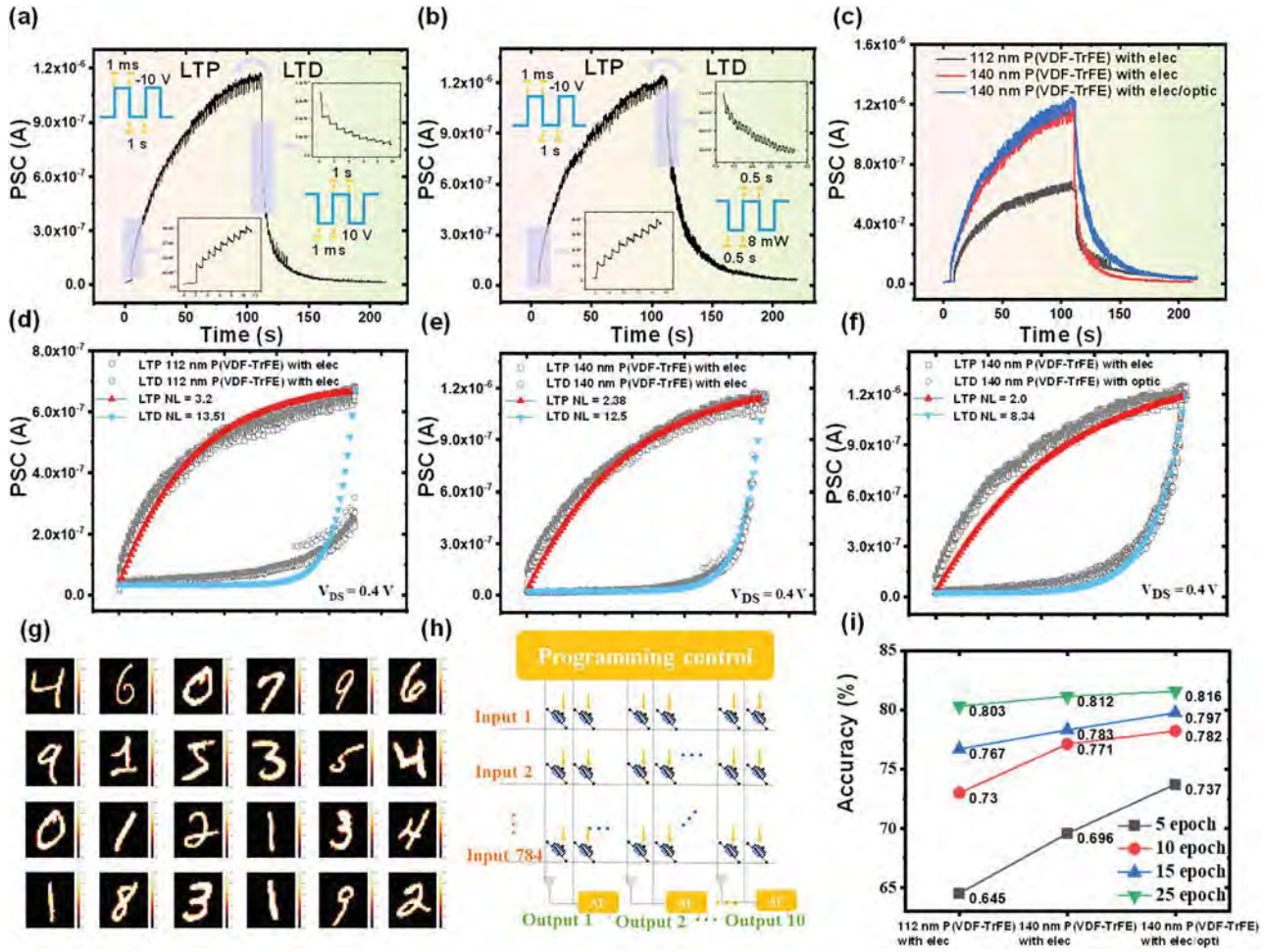

Fig. 5. LTP/LTD characteristics and HNNs of P(VDF-TrFE) film wrapped InGaAs NW artificial synapses. LTP/LTD characteristics realized by (a) electric pulses (b) electric and visible light pulses of devices with a 140 nm thick P(VDF-TrFE) film. (c) The three different LTP/LTD characteristics. The fitted curves and NL values of LTP/LTD characteristics realized by electric pulses with the (d) 112 nm thick and (e) 140 nm thick P(VDF-TrFE) film devices. (f) The fitted curves and NL values of LTP/LTD characteristics realized by electric and visible light pulses with the 140 nm thick P(VDF-TrFE) film device. (g) Supervised learning on the MNIST database. (h) Demonstration of the SLP artificial neural network. (i) The training process of the corresponding three LTP/LTD characteristics.

modulated by 100 continuous depression visible light pulses. The LTP/LTD data are then collected and compiled in Fig. 5d–f with the curve fitting that employs the following formula [59]:

$$G_P = B\left(1 - e^{\left(-\frac{P}{A}\right)}\right) + G_{min} \quad (1)$$

$$G_D = -B\left(1 - e^{\left(\frac{P-P_{max}}{A}\right)}\right) + G_{max} \quad (2)$$

$$B = \frac{G_{max} - G_{min}}{1 - e^{\frac{-P_{max}}{A}}} \quad (3)$$

where G_{max}, G_{min} and P_{max} are directly extracted from the experimental data, representing the maximum weight, minimum weight and the maximum number of pulses required to switch the device between the minimum and maximum weights, respectively. The value of 100/A is redefined as a nonlinearity (NL) parameter. This way, when the NL value is closer to 0, the regulation behaviors of conductance will become more linear and vice versa (Fig. S20). On the one hand, for devices of different P(VDF-TrFE) thickness, the LTP's NL values have an obvious difference (Fig. 5d and e). Since the thicker ferroelectric film has the more ferroelectric domains, under continuous pulses of constant intensity, the intensity of polarized electric field generated by the ferroelectric film is more likely to change linearly. For devices using different depression stimulation with the same P(VDF-TrFE) film (Fig. 5e and f), the LTD's NL values of the device with visible light pulses is significantly lower. The fitted NL data are as well compiled in Fig. S21a. Important, LTP and LTD are essential for the implementation of low-power neuromorphic computing [60,61]. However, when the linearity is at a low level, the pulse numbers will be dominating. Therefore, an increase in one-sided-level numbers can eventually reduce the harmful influence of nonlinearity, which means that the low nonlinearity makes it appealing to achieve the better computation accuracy [62].

At the same time, the weight updating in HNNs can be determined from the LTP/LTD characteristic curves, which are strongly dependent on the number of pulses and the NL values. In order to make metadata effectively train the model in HNNs and solve the problems of narrow weight distribution, the normalized conductance value calculated by the following formula:

$$G_{norm} = \frac{G_n - G_{min}}{G_{max} - G_{min}} \quad (4)$$

where G_{norm} is conductance after normalization, G_n is conductance values of the current state, G_{min} and G_{max} are the maximum conductance and minimum conductance, respectively, are employed. To be specific, the normalized conductance of devices is shown in Fig. S21b, which will be used for the HNNs weight update algorithm subsequently investigated. A HNN was simulated for the supervised learning on the MNIST (Modified National Institute of Standards and Technology) database (Fig. 5g) [63,64]. A single layer perceptron (SLP) HNN with 784 input neurons and 10 output neurons was used for the simulation as shown in Fig. 5h. The HNN algorithm with an analog weight updating was exploited in the simulation by inputting the conductance modulation properties [65]. The 784 input neurons correspond to 28 × 28 pixels of the MNIST image data, while the 10 output neurons link to 10 classes of digits (0–9). Technically, the update algorithm employs the method of unidirection with the flowchart compiled to illustrate the training procedure in Fig. S22 [66]. The training process is also shown in Fig. S23 with all the detailed "counted" data presented in Fig. 5i and the accuracy of training is finally over 80%. Moreover, the synaptic device with a 140 nm thick P(VDF-TrFE) film would achieve the training effect with the less training times. Considering the quest of ultralow power consumption of the ferroelectric wrapped NW synaptic devices, the fewer training times can substantially reduce the power consumption in the supervised learning process, which indicates the great application potential of our devices in the neuromorphic computing technology.

In order to illustrate the practical utilization, the classical Pavlovian conditioning, also known as a simple associative learning, can be successfully realized by the P(VDF-TrFE) wrapped InGaAs NW synaptic devices [67]. Owing to the light response in the infrared band of InGaAs NWs, both electrical and infrared pulses could be adopted to mimic the associative learning [68]. As discussed above, the electrical pulses can trigger the P(VDF-TrFE) film to generate a polarized electric field to induce the EPSC behavior. In explicit, the electrical pulses applied at the gate can emulate food (unconditioned stimulus, US) to activate salivation, which is defined as an unconditioned response (UR). Meanwhile, the stimulation with infrared pulses were adopted as the bell (conditioned stimulus, CS) to stimulate a conditioned response (CR). The details of two different stimulations and the infrared response of the synaptic device are shown in Fig. 6a and b. During the synergistic photoelectric modulation, the CS is completely covered by the US to achieve the associative learning process [69]. Similar to the previous works [70,71], when the bell ring was imitated by a series of infrared pulses in the first time, as depicted in Fig. 6c, the salivation simulated by EPSC is not activated (EPSC < 85 nA). However, after combining the stimulation of bell and food, the EPSC would increase above the threshold and the dog will salivate after hearing the ring. When the single stimulation of food was adopted, the EPSC will return to the same level (~ 80 nA) as the final training after a relatively short relaxation time. Furthermore, the mixing stimulation is used again to strengthen the effect of learning. It is obvious that the EPSC is higher than that of the initial training and the salivation is triggered by bell successfully after a longer relaxation time, which infers that the association between CS and US can be sustained for a long time.

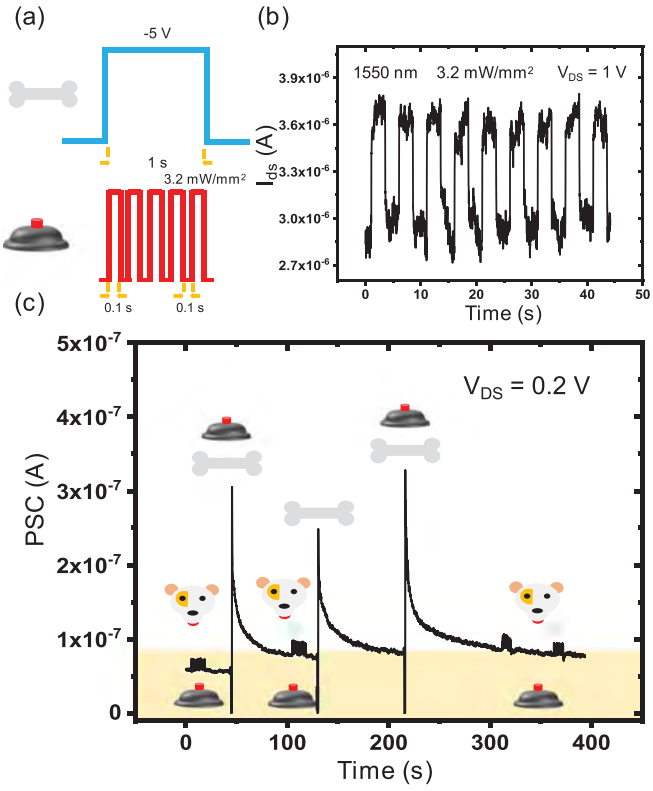

Fig. 6. The mimicking of Pavlovian conditioning by synergistic photoelectric modulation. (a) The combination of electrical and infrared pulses. (b) The response in the infrared band of synaptic devices. (c) Mimicking the Pavlovian conditioning through electrical and infrared pulses.

3. Experimental section

3.1. Synthesis and characterization of nanowires

InGaAs nanowires were synthesized on SiO_2/Si wafer pieces (50 nm thick thermally grown oxide) in a two-zone horizontal tube furnace using a chemical vapor transport method. The mixed InAs and GaAs powders (with the ratio of 1:9 in wt%) were loaded into a boron nitride crucible at the upstream zone of the furnace. The growth substrate pre-deposited with a 0.5 nm thick (nominal thickness) Au film as the catalyst was set at the downstream zone. The temperature of the downstream zone was first elevated to 800 °C and kept for 10 min. Then, the temperature of the downstream zone was cooled directly to the growth temperature (660 °C). When the source temperature reached the designated value (820 °C), the first nucleation step began. After 1–2 min, the downstream was stopped with the heating and then cooled to a second step growth temperature (580 °C). Finally, the second step growth lasted for 40 min. The hydrogen (99.9995%) was used as a carrier gas during the entire growth process with the flowrate maintained at 100 sccm.

3.2. Synaptic NW FET fabrication and characterization

Drop-casting was adopted to disperse the NWs on the Si/SiO_2 substrate. Photolithography was utilized to define the source and drain regions, while 50 nm thick Ni was thermally deposited as the top electrodes followed by the lift-off process. The P(VDF-TrFE) with a molar ratio of 70%/30% was dissolved in diethylcarbonate with the concentration of 25 mg/ml. The thickness of P(VDF-TrFE) film was controlled by number of cycles of the spin-coating process and every spin-coating process had the fixed parameters of 3500 rpm for 20 s. Four different film thickness were corresponded to one to four cycles of spin-coating process. All P(VDF-TrFE) films were annealed at 115 °C for 10 min and 135 °C for 4 h after every spin-coating process. The electrical performance of the P(VDF-TrFE) wrapped InGaAs FET was then characterized with an Agilent 4155 C semiconductor analyzer (Agilent Technologies, Santa Clara, CA). The morphologies and EDS mapping of as-prepared NWs were examined using scanning electron microscopy (SEM, Quanta 450 FEG, FEI) and high-resolution transmission electron microscopy (HRTEM, Thermo Scientific, Talos F200X). The crystallinity and morphologies with different thickness of P(VDF-TrFE) films was confirmed by XRD (D2 Phaser with Cu Kα radiation, Bruker) and atomic force microscopy (Bruker Dimension Icon AFM).

4. Conclusion

In summary, the ferroelectric P(VDF-TrFE) wrapped InGaAs NW artificial synapses capable to operate with the subfemtojoule power consumption per synaptic event is presented. It is demonstrated that the essential bio-synaptic behaviors, such as PPF and EPSC, can be reliably mimicked and effectively modulated through adjusting the thickness of P(VDF-TrFE) films. More importantly, as compared with the pure electric modulation, visible and infrared lights are introduced separately to achieve the more linear LTD characteristic as well as the Pavlov's associative leaning via negative and positive photoconductivity, respectively. Furthermore, the more linear LTP/LTD characteristics can lead to the supervised learning process (accuracy $>$ 80%) with the fewer training times, substantially reducing the energy consumption. Evidently, the synergistic photoelectric modulation is introduced into the ferroelectric wrapped InGaAs NW artificial synapses for the ultralow-power operation, which shows the promising potentials for neuromorphic computing systems based on low-dimensional nanomaterials.

CRediT authorship contribution statement

Pengshan Xie: Conceptualization, Methodology, Validation, Formal analysis, Resources, Data curation, Writing – original draft. **Yulong Huang:** Software, Validation, Resources, Data curation, Writing – original draft. **Wei Wang:** Methodology, Formal analysis, Resources, Validation. **You Meng:** Conceptualization, Methodology, Resources, Validation. **Zhengxun Lai:** Methodology, Resources. **Fei Wang:** Methodology, Resources. **SenPo Yip:** Methodology, Resources. **Xiuming Bu**: Methodology, Resources. **Weijun Wang:** Resources. **Dengji Li:** Resources. **Jia Sun:** Conceptualization, Validation, Resources. **Johnny C. Ho:** Conceptualization, Validation, Formal analysis, Writing – review & editing, Supervision, Resources, Project administration.

Declaration of Competing Interest

The authors declare that they have no known competing financial interests or personal relationships that could have appeared to influence the work reported in this paper.

Acknowledgements

We acknowledge the RGC Research Fellow Scheme (RFS2021-1S04) and the Theme based Research Scheme (T42-103/16-N) of the Research Grants Council of Hong Kong SAR, China, as well as the Foshan Innovative and Entrepreneurial Research Team Program, China (NO. 2018IT100031).

Appendix A. Supporting information

Supplementary data associated with this article can be found in the online version at doi:10.1016/j.nanoen.2021.106654.

References

[1] M.A. Zidan, J.P. Strachan, W.D. Lu, The future of electronics based on memristive systems, Nat. Electron. 1 (2018) 22–29.
[2] V.K. Sangwan, M.C. Hersam, Neuromorphic nanoelectronic materials, Nat. Nanotechnol. 15 (2020) 517–528.
[3] S. Seo, S.-H. Jo, S. Kim, J. Shim, S. Oh, J.-H. Kim, K. Heo, J.-W. Choi, C. Choi, S. Oh, D. Kuzum, H.S.P. Wong, J.-H. Park, Artificial optic-neural synapse for colored and color-mixed pattern recognition, Nat. Commun. 9 (2018) 5106.
[4] M.-K. Kim, I.-J. Kim, J.-S. Lee, CMOS-compatible ferroelectric NAND flash memory for high-density, low-power, and high-speed three-dimensional memory, Sci. Adv. 7 (2021) 1341.
[5] Z. Wang, L. Wang, M. Nagai, L. Xie, M. Yi, W. Huang, Nanoionics-enabled memristive devices: strategies and materials for neuromorphic applications, Adv. Electron. Mater. 3 (2017), 1600510.
[6] P.A. Merolla, J.V. Arthur, R. Alvarez-Icaza, A.S. Cassidy, J. Sawada, F. Akopyan, B. L. Jackson, N. Imam, C. Guo, Y. Nakamura, B. Brezzo, I. Vo, S.K. Esser, R. Appuswamy, B. Taba, A. Amir, M.D. Flickner, W.P. Risk, R. Manohar, D. S. Modha, A million spiking-neuron integrated circuit with a scalable communication network and interface, Science 345 (2014) 668–673.
[7] Y. LeCun, Y. Bengio, G. Hinton, Deep learning, Nature 521 (2015) 436–444.
[8] W. Zhang, B. Gao, J. Tang, P. Yao, S. Yu, M.-F. Chang, H.-J. Yoo, H. Qian, H. Wu, Neuro-inspired computing chips, Nat. Electron. 3 (2020) 371–382.
[9] E.J. Fuller, S.T. Keene, A. Melianas, Z. Wang, S. Agarwal, Y. Li, Y. Tuchman, C. D. James, M.J. Marinella, J.J. Yang, A. Salleo, A.A. Talin, Parallel programming of an ionic floating-gate memory array for scalable neuromorphic computing, Science 364 (2019) 570–574.
[10] M. Zhang, Z. Tang, X. Liu, J. Van der Spiegel, Electronic neural interfaces, Nat. Electron. 3 (2020) 191–200.
[11] Y. Lee, H.-L. Park, Y. Kim, T.-W. Lee, Organic electronic synapses with low energy consumption, Joule 5 (2021) 794–810.
[12] S. Jang, S. Jang, E.-H. Lee, M. Kang, G. Wang, T.-W. Kim, Ultrathin conformable organic artificial synapse for wearable intelligent device applications, ACS Appl. Mater. Interfaces 11 (2019) 1071–1080.
[13] S. Ham, M. Kang, S. Jang, J. Jang, S. Choi, T.-W. Kim, G. Wang, One-dimensional organic artificial multi-synapses enabling electronic textile neural network for wearable neuromorphic applications, Sci. Adv. 6 (2020) 1178.
[14] M. Carroli, A.G. Dixon, M. Herder, E. Pavlica, S. Hecht, G. Bratina, E. Orgiu, P. Samorì, Multiresponsive nonvolatile memories based on optically switchable ferroelectric organic field-effect transistors, Adv. Mater. 33 (2021), 2007965.

[15] E. Li, X. Wu, Q. Chen, S. Wu, L. He, R. Yu, Y. Hu, H. Chen, T. Guo, Nanoscale channel organic ferroelectric synaptic transistor array for high recognition accuracy neuromorphic computing, Nano Energy 85 (2021), 106010.

[16] S. Kim, K. Heo, S. Lee, S. Seo, H. Kim, J. Cho, H. Lee, K.-B. Lee, J.-H. Park, Ferroelectric polymer-based artificial synapse for neuromorphic computing, Nanoscale. Horiz. 6 (2021) 139–147.

[17] B. Tian, C.M. Lieber, Nanowired bioelectric interfaces, Chem. Rev. 119 (2019) 9136–9152.

[18] I. Sanchez Esqueda, X. Yan, C. Rutherglen, A. Kane, T. Cain, P. Marsh, Q. Liu, K. Galatsis, H. Wang, C. Zhou, Aligned carbon nanotube synaptic transistors for large-scale neuromorphic computing, ACS Nano 12 (2018) 7352–7361.

[19] C. Jia, Z. Lin, Y. Huang, X. Duan, Nanowire electronics: from nanoscale to macroscale, Chem. Rev. 119 (2019) 9074–9135.

[20] J.J. Hou, F. Wang, N. Han, F. Xiu, S. Yip, M. Fang, H. Lin, T.F. Hung, J.C. Ho, Stoichiometric effect on electrical, optical, and structural properties of composition-tunable $In_xGa_{1-x}As$ nanowires, ACS Nano 6 (2012) 9320–9325.

[21] J.J. Hou, N. Han, F. Wang, F. Xiu, S. Yip, A.T. Hui, T. Hung, J.C. Ho, Synthesis and characterizations of ternary InGaAs nanowires by a two-step growth method for high-performance electronic devices, ACS Nano 6 (2012) 3624–3630.

[22] A. Klamchuen, M. Suzuki, K. Nagashima, H. Yoshida, M. Kanai, F. Zhuge, Y. He, G. Meng, S. Kai, S. Takeda, T. Kawai, T. Yanagida, Rational concept for designing vapor–liquid–solid growth of single crystalline metal oxide nanowires, Nano Lett. 15 (2015) 6406–6412.

[23] J. Sun, Y. Yin, M. Han, Z.-x Yang, C. Lan, L. Liu, Y. Wang, N. Han, L. Shen, X. Wu, J. C. Ho, , Nonpolar-oriented wurtzite InP nanowires with electron mobility approaching the theoretical limit, ACS Nano 12 (2018) 10410–10418.

[24] Z.-x Yang, L. Liu, S. Yip, D. Li, L. Shen, Z. Zhou, N. Han, T.F. Hung, E.Y.-B. Pun, X. Wu, A. Song, J.C. Ho, Complementary metal oxide semiconductor-compatible, high-mobility, <111>-oriented GaSb nanowires enabled by vapor-solid-solid chemical vapor deposition, ACS Nano 11 (2017) 4237–4246.

[25] Z. Zhu, M. Suzuki, K. Nagashima, H. Yoshida, M. Kanai, G. Meng, H. Anzai, F. Zhuge, Y. He, M. Boudot, S. Takeda, T. Yanagida, Rational concept for reducing growth temperature in vapor–liquid–solid process of metal oxide nanowires, Nano Lett. 16 (2016) 7495–7502.

[26] X. Wang, Y. Chen, G. Wu, D. Li, L. Tu, S. Sun, H. Shen, T. Lin, Y. Xiao, M. Tang, W. Hu, L. Liao, P. Zhou, J. Sun, X. Meng, J. Chu, J. Wang, Two-dimensional negative capacitance transistor with polyvinylidene fluoride-based ferroelectric polymer gating, npj 2D Mater. Appl. 1 (2017) 38.

[27] H.-Y. Cheung, S. Yip, N. Han, G. Dong, M. Fang, Z.-x Yang, F. Wang, H. Lin, C.-Y. Wong, J.C. Ho, Modulating electrical properties of InAs nanowires via molecular monolayers, ACS Nano 9 (2015) 7545–7552.

[28] C. Lan, S. Yip, X. Kang, Y. Meng, X. Bu, J.C. Ho, Gate bias stress instability and hysteresis characteristics of InAs nanowire field-effect transistors, ACS Appl. Mater. Interfaces 12 (2020) 56330–56337.

[29] A.C. Ford, J.C. Ho, Y.-L. Chueh, Y.-C. Tseng, Z. Fan, J. Guo, J. Bokor, A. Javey, Diameter-Dependent electron mobility of InAs nanowires, Nano Lett. 9 (2009) 360–365.

[30] F. Wang, S. Yip, N. Han, K. Fok, H. Lin, J.J. Hou, G. Dong, T. Hung, K.S. Chan, J. C. Ho, Surface roughness induced electron mobility degradation in InAs nanowires, Nanotechnology 24 (2013), 375202.

[31] M. Kang, S.-A. Lee, S. Jang, S. Hwang, S.-K. Lee, S. Bae, J.-M. Hong, S.H. Lee, K.-U. Jeong, J.A. Lim, T.-W. Kim, Low-voltage organic transistor memory fiber with a nanograined organic ferroelectric film, ACS Appl. Mater. Interfaces 11 (2019) 22575–22582.

[32] J. Hafner, S. Benaglia, F. Richheimer, M. Teuschel, F.J. Maier, A. Werner, S. Wood, D. Platz, M. Schneider, K. Hradil, F.A. Castro, R. Garcia, U. Schmid, Multi-scale characterisation of a ferroelectric polymer reveals the emergence of a morphological phase transition driven by temperature, Nat. Commun. 12 (2021) 152.

[33] Q. Hang, F. Wang, P.D. Carpenter, D. Zemlyanov, D. Zakharov, E.A. Stach, W. E. Buhro, D.B. Janes, Role of molecular surface passivation in electrical transport properties of InAs nanowires, Nano Lett. 8 (2008) 49–55.

[34] S.K. Hwang, I. Bae, R.H. Kim, C. Park, Flexible non-volatile ferroelectric polymer memory with gate-controlled multilevel operation, Adv. Mater. 24 (2012) 5910–5914.

[35] S.J. Kang, I. Bae, Y.J. Park, T.H. Park, J. Sung, S.C. Yoon, K.H. Kim, D.H. Choi, C. Park, Non-volatile ferroelectric poly(vinylidene fluoride-co-trifluoroethylene) memory based on a single-crystalline tri-isopropylsilylethynyl pentacene field-effect transistor, Adv. Funct. Mater. 19 (2009) 1609–1616.

[36] Y.T. Lee, H. Kwon, J.S. Kim, H.-H. Kim, Y.J. Lee, J.A. Lim, Y.-W. Song, Y. Yi, W.-K. Choi, D.K. Hwang, S. Im, Nonvolatile ferroelectric memory circuit using black phosphorus nanosheet-based field-effect transistors with P(VDF-TrFE) polymer, ACS Nano 9 (2015) 10394–10401.

[37] N. Park, H. Kang, J. Park, Y. Lee, Y. Yun, J.-H. Lee, S.-G. Lee, Y.H. Lee, D. Suh, Ferroelectric single-crystal gated graphene/hexagonal-BN/ferroelectric field-effect transistor, ACS Nano 9 (2015) 10729–10736.

[38] N. Rusk, Deep learning, Nat. Methods 13 (2016) 35.

[39] L.F. Abbott, W.G. Regehr, Synaptic computation, Nature 431 (2004) 796–803.

[40] T. Ohno, T. Hasegawa, T. Tsuruoka, K. Terabe, J.K. Gimzewski, M. Aono, Short-term plasticity and long-term potentiation mimicked in single inorganic synapses, Nat. Mater. 10 (2011) 591–595.

[41] L.Q. Zhu, C.J. Wan, L.Q. Guo, Y. Shi, Q. Wan, Artificial synapse network on inorganic proton conductor for neuromorphic systems, Nat. Commun. 5 (2014) 3158.

[42] S. Dai, X. Wu, D. Liu, Y. Chu, K. Wang, B. Yang, J. Huang, Light-stimulated synaptic devices utilizing interfacial effect of organic field-effect transistors, ACS Appl. Mater. Interfaces 10 (2018) 21472–21480.

[43] H.-L. Park, Y. Lee, N. Kim, D.-G. Seo, G.-T. Go, T.-W. Lee, Flexible neuromorphic electronics for computing, soft robotics, and neuroprosthetics, Adv. Mater. 32 (2020), 1903558.

[44] D. Kuzum, S. Yu, H.S. Philip Wong, Synaptic electronics: materials, devices and applications, Nanotechnology 24 (2013), 382001.

[45] W. Xu, S.-Y. Min, H. Hwang, T.-W. Lee, Organic core-sheath nanowire artificial synapses with femtojoule energy consumption, Sci. Adv. 2 (2016), 1501326.

[46] Y. van de Burgt, E. Lubberman, E.J. Fuller, S.T. Keene, G.C. Faria, S. Agarwal, M. J. Marinella, A. Alec Talin, A. Salleo, A non-volatile organic electrochemical device as a low-voltage artificial synapse for neuromorphic computing, Nat. Mater. 16 (2017) 414–418.

[47] J. Zhao, Z. Zhou, Y. Zhang, J. Wang, L. Zhang, X. Li, M. Zhao, H. Wang, Y. Pei, Q. Zhao, Z. Xiao, K. Wang, C. Qin, G. Wang, H. Li, B. Ding, F. Yan, K. Wang, D. Ren, B. Liu, X. Yan, An electronic synapse memristor device with conductance linearity using quantized conduction for neuroinspired computing, J. Mater. Chem. C 7 (2019) 1298–1306.

[48] P. Feng, W. Xu, Y. Yang, X. Wan, Y. Shi, Q. Wan, J. Zhao, Z. Cui, Printed neuromorphic devices based on printed carbon nanotube thin-film transistors, Adv. Funct. Mater. 27 (2017), 1604447.

[49] S. Wang, L. Liu, L. Gan, H. Chen, X. Hou, Y. Ding, S. Ma, D.W. Zhang, P. Zhou, Two-dimensional ferroelectric channel transistors integrating ultra-fast memory and neural computing, Nat. Commun. 12 (2021) 53.

[50] Y. Fu, L.-a Kong, Y. Chen, J. Wang, C. Qian, Y. Yuan, J. Sun, Y. Gao, Q. Wan, Flexible neuromorphic architectures based on self-supported multiterminal organic transistors, ACS Appl. Mater. Interfaces 10 (2018) 26443–26450.

[51] R.A. John, N. Tiwari, C. Yaoyi, Ankit N. Tiwari, M. Kulkarni, A. Nirmal, A. C. Nguyen, A. Basu, N. Mathews, Ultralow power dual-gated subthreshold oxide neuristors: an enabler for higher order neuronal temporal correlations, ACS Nano 12 (2018) 11263–11273.

[52] Y. Meng, F. Li, C. Lan, X. Bu, X. Kang, R. Wei, S. Yip, D. Li, F. Wang, T. Takahashi, T. Hosomi, K. Nagashima, T. Yanagida, J.C. Ho, Artificial visual systems enabled by quasi–two-dimensional electron gases in oxide superlattice nanowires, Sci. Adv. 6 (2020) 6389.

[53] S. Gao, G. Liu, H. Yang, C. Hu, Q. Chen, G. Gong, W. Xue, X. Yi, J. Shang, R.-W. Li, An oxide Schottky junction artificial optoelectronic synapse, ACS Nano 13 (2019) 2634–2642.

[54] T. Chang, S.-H. Jo, W. Lu, Short-term memory to long-term memory transition in a nanoscale memristor, ACS Nano 5 (2011) 7669–7676.

[55] L. Shen, S. Yip, C. Lan, L. Shu, D. Li, Z. Zhou, C.-Y. Wong, E.Y.B. Pun, J.C. Ho, Enhanced negative photoconductivity in inas nanowire phototransistors surface-modified with molecular monolayers, Adv. Mater. Interfaces 5 (2018), 1701104.

[56] J. Chen, C.H. Yang, R.A. Wilson, M.J. Yang, Observation of negative persistent photoconductivity in an n-channel GaAs/AlxGa1−xAs single heterojunction, Appl. Phys. Lett. 60 (1992) 2113–2115.

[57] N. Guo, W. Hu, L. Liao, S. Yip, J.C. Ho, J. Miao, Z. Zhang, J. Zou, T. Jiang, S. Wu, X. Chen, W. Lu, Anomalous and highly efficient InAs nanowire phototransistors based on majority carrier transport at room temperature, Adv. Mater. 26 (2014) 8203–8209.

[58] Y. Han, M. Fu, Z. Tang, X. Zheng, X. Ji, X. Wang, W. Lin, T. Yang, Q. Chen, Switching from negative to positive photoconductivity toward intrinsic photoelectric response in InAs nanowire, ACS Appl. Mater. Interfaces 9 (2017) 2867–2874.

[59] P. Chen, X. Peng, S. Yu, NeuroSim+: an integrated device-to-algorithm framework for benchmarking synaptic devices andarray architectures, in: Proceedings of the IEEE IEDM. 2017, 6.1.1–6.1.4.

[60] M. Jerry, S. Dutta, A. Kazemi, K. Ni, J. Zhang, P.-Y. Chen, P. Sharma, S. Yu, X.S. Hu, M. Niemier, A ferroelectric field effect transistor based synaptic weight cell, J. Phys. D Appl. Phys. 51 (2018), 434001.

[61] C.S. Yang, D.S. Shang, N. Liu, E.J. Fuller, S. Agrawal, A.A. Talin, Y.Q. Li, B.G. Shen, Y. Sun, All-solid-state synaptic transistor with ultralow conductance for neuromorphic computing, Adv. Funct. Mater. 28 (2018), 1804170.

[62] Y. Xi, B. Gao, J. Tang, A. Chen, M.-F. Chang, X.S. Hu, J. Van Der Spiegel, H. Qian, H. Wu, In-memory learning with analog resistive switching memory: a review and perspective, Proc. IEEE 109 (2020) 14–42.

[63] L. Deng, The mnist database of handwritten digit images for machine learning research, IEEE Signal. Proc. Mag. 29 (2012) 141–142.

[64] X.-X. Niu, C.Y. Suen, A novel hybrid CNN–SVM classifier for recognizing handwritten digits, Pattern Recogn. 45 (2012) 1318–1325.

[65] J. Sun, S. Oh, Y. Choi, S. Seo, M.J. Oh, M. Lee, W.B. Lee, P.J. Yoo, J.H. Cho, J. H. Park, Optoelectronic synapse based on igzo-alkylated graphene oxide hybrid structure, Adv. Funct. Mater. 28 (2018), 1804397.

[66] C. Qian, S. Oh, Y. Choi, J.-H. Kim, J. Sun, H. Huang, J. Yang, Y. Gao, J.-H. Park, J. H. Cho, Solar-stimulated optoelectronic synapse based on organic heterojunction with linearly potentiated synaptic weight for neuromorphic computing, Nano Energy 66 (2019), 104095.

[67] C. Wu, T.W. Kim, T. Guo, F. Li, D.U. Lee, J.J. Yang, Mimicking classical conditioning based on a single flexible memristor, Adv. Mater. 29 (2017), 1602890.

[68] H. Zhang, W. Wang, S. Yip, D. Li, F. Li, C. Lan, F. Wang, C. Liu, J.C. Ho, Enhanced performance of near-infrared photodetectors based on InGaAs nanowires enabled by a two-step growth method, J. Mater. Chem. C 8 (2020) 17025–17033.

[69] X. Ji, B.D. Paulsen, G.K.K. Chik, R. Wu, Y. Yin, P.K.L. Chan, J. Rivnay, Mimicking associative learning using an ion-trapping non-volatile synaptic organic electrochemical transistor, Nat. Commun. 12 (2021) 2480.
[70] Y. Chen, W. Qiu, X. Wang, W. Liu, J. Wang, G. Dai, Y. Yuan, Y. Gao, J. Sun, Solar-blind SnO_2 nanowire photo-synapses for associative learning and coincidence detection, Nano Energy 62 (2019) 393–400.
[71] J.-L. Meng, T.-Y. Wang, L. Chen, Q.-Q. Sun, H. Zhu, L. Ji, S.-J. Ding, W.-Z. Bao, P. Zhou, D.W. Zhang, Energy-efficient flexible photoelectric device with 2D/0D hybrid structure for bio-inspired artificial heterosynapse application, Nano Energy 83 (2021), 105815.

Pengshan Xie is currently a Ph.D. student in the Department of Materials Science and Engineering at the City University of Hong Kong. He received his BS and MS degree from Central South University in 2017 and 2020, respectively. His research interests mainly focus on the fabrication of nanomaterials, including III-V semiconductor nanowires, novel neuromorphic electronics and field-effect transistors, etc.

Yulong Huang received an MS degree from Central South University in 2021. At present, he is a research assistant at Central South University. His research interests are focused on neuromorphic (neuro-inspired) computing and algorithm of arrays with neuromorphic devices.

Wei Wang is currently a Ph.D. student in the Department of Materials Science and Engineering at the City University of Hong Kong. He received his BS degree in Electronic Science and Technology from Anhui Jianzhu University in 2012 and an MS degree in Materials Engineering from Tongji University in 2015. His research mainly involves the fabrication of nanomaterials, including III-V semiconductor nanowires and 2D materials, along with nanomaterials-based devices regarding the integration of field-effect transistors and near-infrared photoconductors/photodiodes, etc.

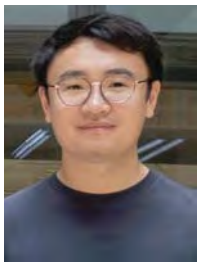

You Meng is working as a postdoctoral researcher in the Department of Materials Science and Engineering at the City University of Hong Kong. He received his BS and MS degree in Physics from the Qingdao University in 2015 and 2018, respectively, and a Ph.D. degree in Materials Science and Engineering from the City University of Hong Kong in 2021. His research interests mainly focus on nanomaterials-based neuromorphic electronics, photoconductive/photovoltaic photodetectors, field-effect/electrochemical transistors, etc.

Jia Sun received his Ph.D. degree from Hunan University in 2012. He was a postdoctoral researcher at Central South University (2012–2014) and Sungkyunkwan University (2017–2018). In 2014, he joined the faculty at Central South University and is currently a Professor in the School of Physics and Electronics. His research interests focus on novel photoelectronic devices and neuromorphic devices.

Johnny C. Ho is a Professor of Materials Science and Engineering at the City University of Hong Kong. He received his BS degree in Chemical Engineering and his MS and Ph.D. degrees in Materials Science and Engineering from the University of California, Berkeley, in 2002, 2005, and 2009, respectively. From 2009–2010, he was a postdoctoral research fellow in the Nanoscale Synthesis and Characterization Group at Lawrence Livermore National Laboratory. His research interests focus on synthesis, characterization, integration, and device applications of nanoscale materials for various technological applications, including nanoelectronics, sensors, and energy harvesting.